Two types of three-dimensional quantum Hall effects in multilayer WTe_2

Xurui Zhang,[1] Yeonghun Lee,[2,3] Vivek Kakani,[1] Kun Yang,[4] Kyeongjae Cho,[2] and Xiaoyan Shi[1,*]

[1]*Department of Physics, The University of Texas at Dallas, Richardson, Texas 75080, USA*

[2]*Department of Materials Science and Engineering, The University of Texas at Dallas, Richardson, Texas 75080, USA*

[3]*Department of Electronics Engineering, Incheon National University, Incheon 22012, Republic of Korea*

[4]*Department of Physics and National High Magnetic Field Laboratory, Florida State University, Tallahassee, Florida 32306, USA*

(Received 26 December 2022; revised 25 May 2023; accepted 31 May 2023; published 7 June 2023)

Interplay between topological surface states and bulk states gives rise to diverse exotic transport phenomena in topological materials. The recently proposed Weyl orbit in topological semimetals in the presence of magnetic field is a remarkable example. This novel closed magnetic orbit consists of Fermi arcs on two spatially separated sample surfaces which are connected by the bulk chiral zero mode, which can contribute to transport. Here we report Shubnikov–de Haas oscillation and its evolution into quantum Hall effect (QHE) in multilayered type-II Weyl semimetal WTe_2. We observe both the three-dimensional (3D) QHE from bulk states by parallel stacking of confined two-dimensional layers in the low magnetic field region and the 3D QHE in the quantized surface transport due to Weyl orbits in the high magnetic field region. Our study of the two types of QHEs controlled by magnetic field and our demonstration of the crossover between quantized bulk and surface transport provide an essential platform for the future quantized transport studies in topological semimetals.

DOI: 10.1103/PhysRevB.107.245410

I. INTRODUCTION

A two-dimensional electron gas (2DEG) in a perpendicular magnetic field (H) may exhibit the quantum Hall effect (QHE) [1], in which the Hall conductivity σ_{xy} will be quantized at $\nu e^2/h$, where ν is the filling factor, indicating the number of filled Landau levels (LLs) [2,3], and e and h are the electron charge and the Planck constant, respectively. The quantized σ_{xy} always accompanies simultaneously the vanishing longitudinal resistance R_{xx}, indicating dissipationless transport along the chiral edges of 2DEG while maintaining an insulating bulk. As members of a large family of topological quantum states [4], quantization of σ_{xy} in quantum Hall systems reveal the nontrivial topology, with ν being a topological invariant, which is independent of material type and geometry [2,3]. Recently, predicting and realizing the QHE in topological materials have attracted intense interest due to both the rich physics and potential applications in quantum devices. In 3D topological insulator (TI) Bi_2Se_3, the quasi-2D QHE exhibits strong thickness-dependence [5]. In addition, theories suggest that a half-quantized surface Hall conductance representing the topologically nontrivial nature can be induced in TIs [6,7]. Indeed, it has been observed in an intrinsic 3D TI $BiSbTeSe_2$ [8]. Recent theoretical studies predict formation of an exotic orbit, the so-called Weyl orbit (WO), can support QHE in 3D Dirac and Weyl semimetals (DSM/WSM) [9–12]. In such materials, there exist topologically protected surface states that form open Fermi arcs, connecting pairs of bulk Weyl nodes with opposite chiralities [13,14]. In H field, two Fermi arcs on the opposite sample surfaces are connected by bulk chiral modes to form closed WOs [9–12,15–17] which can support the QHE in bulk crystals. There have been some experimental verifications of the QHE in 3D DSM Cd_3As_2 [18].

Tungsten ditelluride (WTe_2), a layered transition metal dichalcogenide material, has attracted a great deal of interests due to its unique topological properties. In the bulk form, WTe_2 is a type-II WSM [19]. Interestingly, its monolayer form is a quantum spin Hall insulator at low charge density (n_e) [20,21]. However, QHE has never been observed in this material due to the limited carrier mobilities (μ) [22–25]. Here we report the observation of two different types of QHE in a multilayer WTe_2 film with low n_e. The bulk states contribute to the 3D QHE, in which thickness-dependent quantization comes from parallel 2DEG conduction channels due to quantum confinement along the normal direction of sample surface. With increasing H, the bulk chiral LL (0^{th} LL) mixes with the surface states that form the Fermi arc, which build up the WOs and yield another 3D QHE in high H.

II. EXPERIMENT

The multilayer WTe_2 flake was obtained by mechanical exfoliation of bulk crystals from HQ graphene. Two pieces of hexagonal boron nitride (hBN) thin flakes were used to encapsulate the WTe_2 flake and transferred onto a silicon substrate with 285 nm SiO_2 coating on surface by dry transfer technique [26]. The hBN flakes prevent the WTe_2 flake from air oxidization [27,28] and provide a cleaner interface to improve μ. A standard e-beam lithography and metal deposition (Pd/Au, 10 nm/50 nm) process was applied to make electrical contacts to a Hall bar sample. The device was then wire bonded and attached to a DIP socket for transport measurements, which were carried out in a dilution refrigerator with a base

*xshi@utdallas.edu

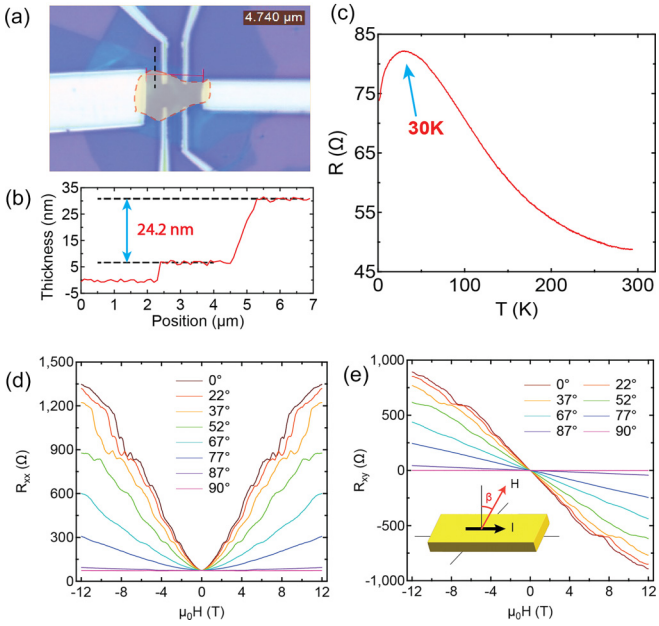

FIG. 1. (a) An optical image of the WTe_2 device. Red scale bar gives the length of channel which is 4.74 μm. Black dashed line guides the AFM measurement. WTe_2 flake is highlighted in orange. (b) Thickness $t = 24.2$ nm was determined by AFM. The first step measures the thickness of the bottom hBN. (c) The anomalous resistance peak in $R_{xx}(T, H = 0)$ occurs around $T_p \approx 30$ K. (d), (e) Angular dependence of R_{xx} and R_{xy} at 20 mK, respectively. Symmetrized data are shown in (d) and (e). The inset in (e) shows the sample, I, and H arrangement. β is the angle labeled in (d) and (e).

temperature (T) of 20 mK. Figure 1(a) shows an optical image of the device with thickness $t = 24.2$ nm, determined by atomic force microscopy (AFM) [Fig. 1(b)].

The band structure of WTe_2 was calculated by the density functional theory (DFT) implemented in the Vienna *Ab initio* Simulation Package [29,30]. The exchange-correlation energy functional was given by the Perdew-Burke-Ernzerhof functional [31] in the generalized gradient approximation. The pseudopotential was given by the projector-augmented wave method [32,33]. The energy cutoff for the plane-wave basis set was 250 eV, and a $7 \times 3 \times 1$ Γ-centered k-point grid was adopted for the Brillouin zone sampling. Spin-orbit coupling was considered. The zero damping DFT-D3 method of Grimme [34] was employed to describe van der Waals interactions. The cell geometry was optimized until the maximum atomic force is smaller than 0.01 eV/Å.

III. RESULTS AND DISCUSSIONS

We first measured the T dependence of the longitudinal resistance $R_{xx}(T)$ at zero H. As shown in Fig. 1(c), unlike the commonly observed $R(T)$ in WTe_2 [22–25], an anomalous peak emerges at ~30 K and separates the metallic ($T < 30$ K) and insulating ($T < 30$ K) behaviors. Such a peak can be ascribed to the T-dependent Fermi energy shift of the electronic band structure. A similar feature in $ZrTe_5$ and $HfTe_5$, 3D quantum Hall materials, has been proved to be caused by changes in carrier types, which is intrinsically due to the T-induced Fermi energy shift of the electronic band structure [35–38]. It can also happen in WTe_2 because of the confirmed Lifshitz transition [39]. For small n_e, insulating behavior dominated by a certain type of carrier could happen. To verify this, elaborate measurements of angle-dependent magnetoresistance (MR) and Hall effect provide further insight into the band-topological properties, as shown in Figs. 1(d) and 1(e), respectively.

Magnetotransport with rotational H is conducted. The current (I) was applied perpendicular to H (z direction), which is applied with an angle (β) with respect to the normal direction (c axis) of the layers [Fig. 1(e) inset]. With $\mu_0 H > 1$ T and $\beta = 0°$, clear SdH oscillations can be identified in MR along with several plateaus in Hall resistance R_{xy}, indicating a QHE in such a high-quality sample with both a low n_e and a high μ. By fitting the low-H linear regime in the Hall measurement and combined with the normal-state R_{xx}, we extract the electron-type $n_e = 3.2 \times 10^{18}$ cm^{-3} and $\mu = 32400$ cm^{-2}/Vs. The n_e (and μ) is at least an order of magnitude lower (and higher) than other WTe_2 flakes [23–25]. As $\beta \neq 0°$, the MR damps with the law of cosines, likely suggesting a 2D nature and a highly anisotropic Fermi surface (FS) with a cigar or ellipsoid shape. This is reasonable for a layered material, and further transport study along the stacking direction is needed to determine the shape of FS. We also found that the absolute resistance values of those plateaus and oscillations are independent of β, which is a hallmark of QHE.

We extracted the R_{xx} oscillations (ΔR_{xx}) at different angles by removing the large positive MR background, which is an intrinsic characteristic in WTe_2 [40]. In Fig. 2(a), ΔR_{xx} exhibits a clear change in periodicity at large fields. The Fourier transformation of the SdH oscillations [Fig. 2(b)] shows higher oscillation frequencies in the large-H region, in addition to the small primary frequency which dominates the low-H region as the only frequency at around 7.5 T. We first focus on the low-H region. A Landau fan diagram is plotted by following maxima (associated with integers) and minima (associated with half-integers) in the SdH oscillations in Fig. 2(c). The oscillation frequency B_F and Berry phase ϕ_B can be extracted according to the Lifshitz-Onsager quantization rule [41]: $\frac{B_F}{B} = N + \gamma = N + \frac{1}{2} - \frac{\phi_B}{2\pi} - \delta$, where $B = \mu_0 H$, N is the LL index, γ is the intercept in the fan diagram, and δ is an additional phase shift determined by the dimensionality, taking the value $\delta = 0$ (or $\pm 1/8$) for 2D (or 3D) case [41]. In addition, for Dirac fermions, a value of $0 < |\gamma| < 1/8$ implies a nontrivial π Berry phase, whereas $|\gamma| \sim 1/2$ represents a trivial ϕ_B [36]. The inset of Fig. 2(c) shows $\gamma(\beta)$. When $\beta = 0°$, the Landau fan diagram yields a γ around 1/8, exhibiting a nontrivial ϕ_B for the detected FS [Fig. 2(d)]. However, as H is further rotated to almost parallel to I ($\beta = 87°$ and 90°), ϕ_B begins to deviate from the nontrivial one and turns to be trivial ($\gamma \sim 1/2$). Such behavior agrees with a weak TI [36], indicating the topological state in WTe_2. Moreover, the exact intercepts at $\pm 1/8$ suggest the 3D nature of the FS, which indicates the unconventional QHE in our sample. In Fig. 2(d), the $B_F(\beta)$ agrees better with 3D case ($B_F^{3D} = B_{F,z} B_{F,\parallel} / \sqrt{(B_{F,z} \sin\beta)^2 + (B_{F,\parallel} \cos\beta)^2}$, $B_{F,i}$ is the frequency of the SdH oscillation in different direction) than a simple $1/\cos\beta$ relationship in 2D, confirming the 3D nature of the FS [36].

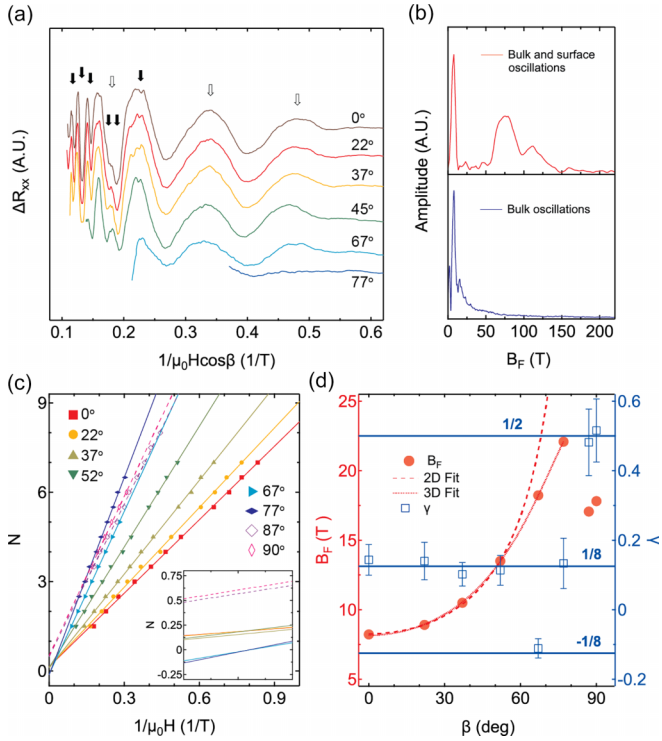

FIG. 2. (a) Angle dependence of ΔR_{xx} versus $1/\mu_0 H\cos\beta$. Curves are shifted vertically for clarity. Hollow and filled arrows denote the bulk and surface oscillations, respectively. (b) Fourier transformation of the SdH oscillations in whole field region (upper) and only low-H region (lower), respectively. (c) Landau fan diagram of SdH oscillations. Lines are linear fit to evaluate the intercepts. Inset is the zoom-in plot near the main plot origin. (d) The angular dependence of (red) oscillation frequency B_F and (blue) intercept γ in (c). Error bars in γ are from the linear fits in (c).

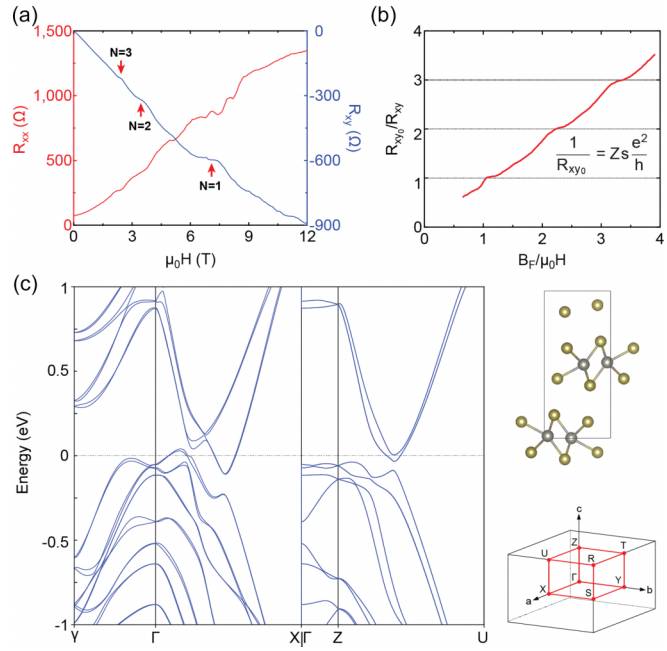

FIG. 3. QHE from bulk. (a) Longitudinal (red) and transverse (blue) MR at 20 mK. The arrows and N mark the quantized plateaus in R_{xy} and oscillation valleys in R_{xx}. (b) Normalized inverse Hall resistance R_{xy_0}/R_{xy} versus B_F/B. (c) DFT band calculation of bulk WTe_2 in zero field. 1% tensile strain along X direction is applied to get the minimum degeneracy factor and reflect the possible strain in real device. The upper inset shows one unit cell of WTe_2, which contains two physical layers. The lower inset shows the orthorhombic Brillouin zone in momentum space.

Let us focus on the QHE in WTe_2. In Fig. 3(a), SdH oscillations and corresponding plateaus can be resolved in both R_{xx} and R_{xy}. N marks the Hall plateau accompanied by an obvious dip in R_{xx}, which provides clear evidence for the QHE. Noticeably, the quantized R_{xy} on the plateau is smaller than the von Klitzing constant h/e^2 by a factor of 42, which applies to all observed plateaus. Such behavior is common in 3D QHE [5,35,36,42,43] and can be simply explained for layered materials by the subbands formed from the quantum confinement along the layer stacking direction. The value of the factor depends on the number of the subbands that are occupied, which is determined by the confinement thickness, and the degeneracy factor [44]. Given the weak band dispersion along the stacking direction in such a van der Waals material, one can expect the number of subbands contributing to the QHE to be the same as the number of layers. Alternatively, one can view the observed QHE as the result of many parallel 2D conduction channels, each acting as a 2DEG, making up the stacking 3D system, which resembles the case in bulk Bi_2Se_3 [5]. We emphasize this does not mean the interlayer hopping is not important here; it is the exact opposite as it is crucial to the topologically nontrivial 3D band structure and the presence of Weyl nodes. To verify our interpretation, we plot normalized inverse Hall resistance R_{xy_0}/R_{xy} versus B_F/B at 20 mK. $1/R_{xy_0}$ is the step size between the consecutive plateaus determined from the plateau values at $\frac{B_F}{B} = 1$ to 3. $1/R_{xy}$ also exhibits clear plateaus at regular intervals of B_F/B, the positions of which nicely correspond to deep minima in R_{xx}. Typically in QHE, this quantization of R_{xy_0}/R_{xy} leads to the normalized filling factor or N. This consists with the plateaus occurring at integer multiples of B_F/B, where a small shift can be attributed to ϕ_B. Such a normalized filling factor is known to stem from the nontrivial π Berry phase of Dirac fermions, which in 2D leads to quantized R_{xy} as follows [42]:

$$\frac{1}{R_{xy}} = \pm s(N+\gamma)\frac{e^2}{h},$$

where s is the degeneracy factor. This gives the successive $1/R_{xy}$ plateau step size as $1/R_{xy_0} = sZ(\frac{e^2}{h})$, Z is the total number of the stacking layers. We have performed a DFT calculation in zero H to investigate s in WTe_2 under applied strain. Under around 2% of uniaxial compressive strain along X direction, the four Weyl points hit the mirror plane and annihilate [19]. Therefore, under the uniaxial tensile strain applied in this work, the four Weyl points move further apart, so the number of Weyl points is not expected to change. Results [Fig. 3(c)] show that under the strain the highly anisotropic electron pocket remains elongated without a closing of the Fermi surface at the Brillouin zone boundary (see the electron pocket at the high-symmetry Z-U line), and s has been reduced from 4 to 2 under the strain. It can be further reduced to 1 with the lift of Kramer's degeneracy in H [45]. In WTe_2, the

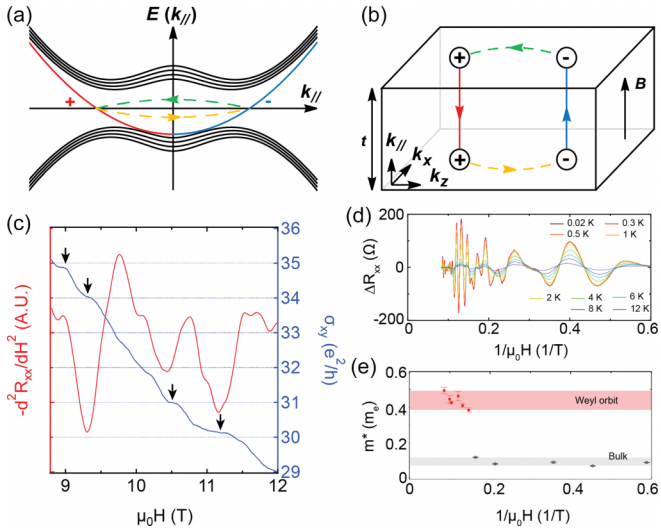

FIG. 4. QHE from Weyl orbits. (a) Schematic plot of energy-band structure in a magnetic field B. $k_{\parallel}$ is the wave vector parallel to B. The red and blue solid curves represent the chiral bulk Landau bands. The yellow (green) dashed curve represents the Fermi arc on the bottom (top) surface. (b) Schematic plot of Weyl orbits in a sample slab with thickness t. Two Fermi arcs on the top and bottom surfaces are interconnected through the bulk chiral zeroth mode. The same colors are used as in (a). (c) QHE measured at high-H region. Second differential of R_{xx} is taken to manifest the SdH oscillations. σ_{xy} is plotted in unit of quantum conductance $\frac{e^2}{h}$. Arrows denote the σ_{xy} plateaus. (d) T dependence of ΔR_{xx}. (e) Extracted m^* of bulk state and Weyl orbit plotted as a function of $1/\mu_0 H$.

spatial-inversion symmetry has already been broken. Then we get $Z = 42 \pm 1$(or $Zs = 42 \pm 1$), where error bar reflects the resistance fluctuations ($\sim$10 Ω) in Hall plateaus, indicating the 3D bulk constitutes 42 layers of 2DEG in parallel. We extract n_e for each parallel 2D conduction channel from the SdH oscillations as $n_{2D}^{\mathrm{SdH}} = \frac{e\ s\ B_F}{h} = 1.91 \times 10^{11}\ \mathrm{cm}^{-2}$. Recall that $n_{3D}^{\mathrm{Hall}} = 3.2 \times 10^{18}\ \mathrm{cm}^{-3}$ from Hall measurement. The ratio between them allows us to predict the effective thickness (t_{2D}) per 2D conduction channel as $t_{2D} = \frac{n_{2D}^{\mathrm{SdH}}}{n_{3D}^{\mathrm{Hall}}} = 0.6$ nm, which is close to but slightly smaller than the theoretical thickness of 1 layer of WTe_2 (0.7 nm). Alternatively, considering the 3D system is made up of 42 layers of conduction channel, we could get the direct measurement of each layer thickness to be $t_{2D} = t/42 = 0.58$ nm from the AFM result, which is surprisingly consistent with the prediction and the Hall resistance. It is, therefore, proved that the 3D QHE in our sample consists of 42 parallel 2D conduction channels, each of which is a physical layer.

Now we focus on the QHE at high-H region (>9 T). In Fig. 2(b), the single oscillation frequency in low-H region corresponds to the 3D bulk FS that has been discussed above. However, much larger oscillation frequencies, corresponding to larger FS, are superimposed on that of the bulk state from high-H region. The integer QHE originated from the bulk state clearly stretch down to the quantum limit with $N = 1$ at around 7 T [Fig. 3(a)]. Therefore, the bulk carriers are already confined to the lowest LL and can no longer produce any quantum oscillations. However, as shown in Fig. 4(c), clear oscillations can be observed in the second order differential $\frac{d^2R_{xx}}{dH^2}$ and several quantized plateaus can be seen corresponding to the oscillation valleys, indicating that the additional QHE observed in the high-H MR is of 2D nature developed from the surface states. As a WSM, although the surface states of WTe_2 exist in the form of open Fermi arcs, which cannot support closed magnetic orbit individually, the bulk chiral zero mode can bridge the Fermi arcs on the opposite surfaces to form closed WOs [9,12]. The schematic plot of the corresponding energy-band structure and the transport behavior of WO in a slab are shown in Figs. 4(a) and 4(b), respectively. The experimental observation of WO has been verified in a DSM Cd_3As_2 [46–49]. Figures 4(d) and 4(e) show $\Delta R_{xx}(T)$ and the effective mass m^* extracted from the fitting by Lifshitz-Kosevich (LK) formula [41]. In the low-H region, m^* is generally below 0.1 m_e (m_e is the electron mass). Such a small m^* agrees well with a previous report [50]. In contrast, in the high-H region, m^* becomes several times larger ($0.4 \sim 0.5 m_e$) for the higher-frequency oscillations. In the LK formula, larger m^* from the surface state results in a quicker decay of the oscillation amplitude. Such behavior of the surface state has been observed in previous transport studies of WO [49,51]. Here the sample mean free path, $l = \frac{\mu m^* v_F}{e} \approx 700$ nm, fulfills the requirement for observing the WO ($l > t$) [9]. In addition, we estimated the oscillation frequency of the WO, F_s, based on the theory [9] $F_s = E_F k_0/(e\pi \bar{v}_F)$, where Fermi energy $E_F = \hbar \bar{v}_F \bar{k}_F$ and Fermi arc separation $k_0 \sim 0.32 \pm 0.02\ \mathrm{nm}^{-1}$ (Ref. [52]). With the measured n_e, we have the average Fermi wave vector $\bar{k}_F = 1.0\ \mathrm{nm}^{-1}$ (assuming a circular 2D FS) and the calculated quantum oscillation caused by WO is 70 T, which agrees well with our experimental observation of ~75 T [Fig. 2(b)]. It also agrees with a reported 78 T in a WTe_2 ribbon [53]. While the surface QHE based on WO occurs at higher fields, the bulk states reach quantum limit and support the WO as an interconnection. This is consistent with recent theoretical work [54,55] suggesting that the Weyl nodes of a WSM are robust and re-emerge under strong H that reorganizes the original bands into Chern bands responsible for the 3D QHE before quantum limit is reached. According to the theory of WO, σ_{xy} depending on both the surface states and the bulk chiral Landau bands can be written as $\sigma_{xy} = \frac{e^2}{h}(n_0 + n)$, where n is an integer and the additional n_0, which originates from the bulk chiral Landau bands, takes the form of $n_0 = \lfloor \frac{k_w t}{\pi} \tan\beta \rfloor$, where k_w is the position of Weyl nodes along B direction in momentum space [12]. In perpendicular B, $n_0 = \tan\beta = 0$ and $n_0 = 0$, σ_{xy} degenerates into the general form $\sigma_{xy} = \frac{ne^2}{h}$. The step size between the consecutive plateaus becomes $\frac{e^2}{h}$, as shown in Fig. 4(c). It is also worth mentioning that the much smaller bulk m^* can very easily induce the quantum confinement and subbands formation along the c axis, thus leading to the 3D QHE in bulk state [44]. That is why the bulk transport is confined in each layer vertically. We believe the Weyl orbits in type-II WSM is likely to be much more complicated than those in DSM and type-I WSM, especially when considering the relative field orientations and the lattice anisotropy. Therefore, more theoretical and experimental works are desired to further clarify the detailed nature of the underlying mechanism of the surface orbits in WTe_2.

ACKNOWLEDGMENTS

This work of X.Z., Y.L., V.K., and X.S. was supported by UT Dallas SPIRe fund (No. 2108630). The work of K.Y. was supported by the National Science Foundation (Grant No. DMR-1932796), and performed at the National High Magnetic Field Laboratory, which is supported by National Science Foundation Cooperative Agreement No. DMR-1644779, and the State of Florida. K.C. was supported by National R&D Program through the National Research Foundation of Korea (NRF) funded by Ministry of Science and ICT(2022M3H4A1A04096496).

[1] K. V. Klitzing, G. Dorda, and M. Pepper, New Method for High-Accuracy Determination of the Fine-Structure Constant Based on Quantized Hall Resistance, Phys. Rev. Lett. **45**, 494 (1980).

[2] R. B. Laughlin, Quantized Hall conductivity in two dimensions, Phys. Rev. B **23**, 5632 (1981).

[3] D. J. Thouless, M. Kohmoto, M. P. Nightingale, and M. den Nijs, Quantized Hall Conductance in a Two-Dimensional Periodic Potential, Phys. Rev. Lett. **49**, 405 (1982).

[4] X. Kou, Y. Fan, and K. L. Wang, Review of quantum Hall trio, J. Phys. Chem. Solids **128**, 2 (2019).

[5] H. Cao, J. Tian, I. Miotkowski, T. Shen, J. Hu, S. Qiao, and Y. P. Chen, Quantized Hall Effect and Shubnikov–de Haas Oscillations in Highly Doped Bi_2Se_3: Evidence for Layered Transport of Bulk Carriers, Phys. Rev. Lett. **108**, 216803 (2012).

[6] L. Fu and C. L. Kane, Topological insulators with inversion symmetry, Phys. Rev. B **76**, 045302 (2007).

[7] H. Zhang, C. X. Liu, X. L. Qi, X. Dai, Z. Fang, and S. C. Zhang, Topological insulators in Bi_2Se_3, Bi_2Te_3, and Sb_2Te_3 with a single Dirac cone on the surface, Nat. Phys. **5**, 438 (2009).

[8] Y. Xu, I. Miotkowski, C. Liu, J. Tian, H. Nam, N. Alidoust, J. Hu, C. K. Shih, M. Z. Hasan, and Y. P. Chen, Observation of topological surface state quantum Hall effect in an intrinsic three-dimensional topological insulator, Nat. Phys. **10**, 956 (2014).

[9] A. C. Potter, I. Kimchi, and A. Vishwanath, Quantum oscillations from surface Fermi arcs in Weyl and Dirac semimetals, Nat. Commun. **5**, 5161 (2014).

[10] C. M. Wang, H.-P. Sun, H.-Z. Lu, and X. C. Xie, 3D Quantum Hall Effect of Fermi Arcs in Topological Semimetals, Phys. Rev. Lett. **119**, 136806 (2017).

[11] H. Z. Lu, 3D quantum Hall effect, Natl. Sci. Rev. **6**, 208 (2019).

[12] H. Li, H. Liu, H. Jiang, and X. C. Xie, 3D Quantum Hall Effect and a Global Picture of Edge States in Weyl Semimetals, Phys. Rev. Lett. **125**, 036602 (2020).

[13] X. Wan, A. M. Turner, A. Vishwanath, and S. Y. Savrasov, Topological semimetal and Fermi-arc surface states in the electronic structure of pyrochlore iridates, Phys. Rev. B **83**, 205101 (2011).

[14] N. P. Armitage, E. J. Mele, and A. Vishwanath, Weyl and Dirac semimetals in three-dimensional solids, Rev. Mod. Phys. **90**, 015001 (2018).

[15] C. Zhang, Y. Zhang, H. Z. Lu, X. C. Xie, and F. Xiu, Cycling Fermi arc electrons with Weyl orbits, Nat. Rev. Phys. **3**, 660 (2021).

[16] X.-X. Zhang and N. Nagaosa, Anisotropic three-dimensional quantum Hall effect and magnetotransport in mesoscopic Weyl semimetals, Nano Lett. **22**, 3033 (2022).

[17] F. Xiong, C. Honerkamp, D. M. Kennes, and T. Nag, Understanding the three-dimensional quantum Hall effect in generic multi-Weyl semimetals, Phys. Rev. B **106**, 045424 (2022).

[18] S. Nishihaya, M. Uchida, Y. Nakazawa, M. Kriener, Y. Taguchi, and M. Kawasaki, Intrinsic coupling between spatially-separated surface Fermi-arcs in Weyl orbit quantum Hall states, Nat. Commun. **12**, 2572 (2021).

[19] A. A. Soluyanov, D. Gresch, Z. Wang, Q. Wu, M. Troyer, X. Dai, and B. A. Bernevig, Type-II Weyl semimetals, Nature (London) **527**, 495 (2015).

[20] X. Qian, J. Liu, L. Fu, and J. Li, Quantum spin Hall effect in two-dimensional transition metal dichalcogenides, Science **346**, 1344 (2014).

[21] S. Wu, V. Fatemi, Q. D. Gibson, K. Watanabe, T. Taniguchi, R. J. Cava, and P. Jarillo-Herrero, Observation of the quantum spin Hall effect up to 100 Kelvin in a monolayer crystal, Science **359**, 76 (2018).

[22] X. Zhang, V. Kakani, J. M. Woods, J. J. Cha, and X. Shi, Thickness dependence of magnetotransport properties of tungsten ditelluride, Phys. Rev. B **104**, 165126 (2021).

[23] Y. Luo, H. Li, Y. M. Dai, H. Miao, Y. G. Shi, H. Ding, A. J. Taylor, D. A. Yarotski, R. P. Prasankumar, and J. D. Thompson, Hall effect in the extremely large magnetoresistance semimetal WTe_2, Appl. Phys. Lett. **107**, 182411 (2015).

[24] J. M. Woods, J. Shen, P. Kumaravadivel, Y. Pang, Y. Xie, G. A. Pan, M. Li, E. I. Altman, L. Lu, and J. J. Cha, Suppression of Magnetoresistance in Thin WTe_2 Flakes by Surface Oxidation, ACS Appl. Mater. Interfaces **9**, 23175 (2017).

[25] X. Zhang, J. M. Woods, J. J. Cha, and X. Shi, Crossover between weak antilocalization and weak localization in few-layer WTe_2: Role of electron-electron interactions, Phys. Rev. B **102**, 115161 (2020).

[26] A. Castellanos-Gomez, M. Buscema, R. Molenaar, V. Singh, L. Janssen, H. S. J. Van Der Zant, and G. A. Steele, Deterministic transfer of two-dimensional materials by all-dry viscoelastic stamping, 2D Mater. **1**, 011002 (2014).

[27] L. Wang, I. Gutiérrez-Lezama, C. Barreteau, N. Ubrig, E. Giannini, and A. F. Morpurgo, Tuning magnetotransport in a compensated semimetal at the atomic scale, Nat. Commun. **6**, 8892 (2015).

[28] V. Fatemi, S. Wu, Y. Cao, L. Bretheau, Q. D. Gibson, K. Watanabe, T. Taniguchi, R. J. Cava, and P. Jarillo-Herrero, Electrically tunable low-density superconductivity in a monolayer topological insulator, Science **362**, 926 (2018).

[29] G. Kresse and J. Furthmüller, Efficiency of ab-initio total energy calculations for metals and semiconductors using a plane-wave basis set, Comput. Mater. Sci. **6**, 15 (1996).

[30] G. Kresse and J. Hafner, *Ab initio* molecular dynamics for liquid metals, Phys. Rev. B **47**, 558 (1993).

[31] J. P. Perdew, K. Burke, and M. Ernzerhof, Generalized Gradient Approximation Made Simple, Phys. Rev. Lett. **77**, 3865 (1996).

[32] P. E. Blöchl, Projector augmented-wave method, Phys. Rev. B **50**, 17953 (1994).

[33] G. Kresse and D. Joubert, From ultrasoft pseudopotentials to the projector augmented-wave method, Phys. Rev. B **59**, 1758 (1999).

[34] S. Grimme, J. Antony, S. Ehrlich, and H. Krieg, A consistent and accurate ab initio parametrization of density functional dispersion correction (DFT-D) for the 94 elements H-Pu, J. Chem. Phys. **132**, 154104 (2010).

[35] Y. Liu, X. Yuan, C. Zhang, Z. Jin, A. Narayan, C. Luo, Z. Chen, L. Yang, J. Zou, X. Wu, S. Sanvito, Z. Xia, L. Li, Z. Wang, and F. Xiu, Zeeman splitting and dynamical mass generation in Dirac semimetal $ZrTe_5$, Nat. Commun. **7**, 12516 (2016).

[36] F. Tang, Y. Ren, P. Wang, R. Zhong, J. Schneeloch, S. A. Yang, K. Yang, P. A. Lee, G. Gu, Z. Qiao, and L. Zhang, Three-dimensional quantum Hall effect and metal–insulator transition in $ZrTe_5$, Nature (London) **569**, 537 (2019).

[37] S. Galeski, X. Zhao, R. Wawrzyńczak, T. Meng, T. Förster, P. M. Lozano, S. Honnali, N. Lamba, T. Ehmcke, A. Markou, Q. Li, G. Gu, W. Zhu, J. Wosnitza, C. Felser, G. F. Chen, and J. Gooth, Unconventional Hall response in the quantum limit of $HfTe_5$, Nat. Commun. **11**, 1 (2020).

[38] P. Wang, Y. Ren, F. Tang, P. Wang, T. Hou, H. Zeng, L. Zhang, and Z. Qiao, Approaching three-dimensional quantum Hall effect in bulk $HfTe_5$, Phys. Rev. B **101**, 161201(R) (2020).

[39] I. Pletikosić, M. N. Ali, A. V. Fedorov, R. J. Cava, and T. Valla, Electronic Structure Basis for the Extraordinary Magnetoresistance in WTe_2, Phys. Rev. Lett. **113**, 216601 (2014).

[40] M. N. Ali, J. Xiong, S. Flynn, J. Tao, Q. D. Gibson, L. M. Schoop, T. Liang, N. Haldolaarachchige, M. Hirschberger, N. P. Ong, and R. J. Large Cava, Nonsaturating magnetoresistance in WTe_2, Nature (London) **514**, 205 (2014).

[41] H. Murakawa, M. S. Bahramy, M. Tokunaga, Y. Kohama, C. Bell, Y. Kaneko, N. Nagaosa, H. Y. Hwang, and Y. Tokura, Detection of Berry's phase in a bulk Rashba semiconductor, Science **342**, 1490 (2013).

[42] H. Masuda, H. Sakai, M. Tokunaga, Y. Yamasaki, A. Miyake, J. Shiogai, S. Nakamura, S. Awaji, A. Tsukazaki, H. Nakao, Y. Murakami, T. H. Arima, Y. Tokura, and S. Ishiwata, Quantum Hall effect in a bulk antiferromagnet $EuMnBi_2$ with magnetically confined two-dimensional Dirac fermions, Sci. Adv. **2**, e1501117 (2016).

[43] S. Hill, S. Uji, M. Takashita, C. Terakura, T. Terashima, H. Aoki, J. S. Brooks, Z. Fisk, and J. Sarrao, Bulk quantum Hall effect in Mo_4O_{11}, Phys. Rev. B **58**, 10778 (1998).

[44] M. Uchida, Y. Nakazawa, S. Nishihaya, K. Akiba, M. Kriener, Y. Kozuka, A. Miyake, Y. Taguchi, M. Tokunaga, N. Nagaosa, Y. Tokura, and M. Kawasaki, Quantum Hall states observed in thin films of Dirac semimetal Cd_3As_2, Nat. Commun. **8**, 1 (2017).

[45] N. Nagaosa, T. Morimoto, and Y. Tokura, Transport, magnetic and optical properties of Weyl materials, Nat. Rev. Mater. **5**, 621 (2020).

[46] C. Zhang, A. Narayan, S. Lu, J. Zhang, H. Zhang, Z. Ni, X. Yuan, Y. Liu, J.-H. Park, E. Zhang, W. Wang, S. Liu, L. Cheng, L. Pi, Z. Sheng, S. Sanvito, and F. Xiu, Evolution of Weyl orbit and quantum Hall effect in Dirac semimetal Cd_3As_2, Nat. Commun. **8**, 1272 (2017).

[47] B.-C. Lin, S. Wang, S. Wiedmann, J.-M. Lu, W.-Z. Zheng, D. Yu, and Z.-M. Liao, Observation of an Odd-Integer Quantum Hall Effect from Topological Surface States in Cd_3As_2, Phys. Rev. Lett. **122**, 036602 (2014).

[48] C. Zhang, Y. Zhang, X. Yuan, S. Lu, J. Zhang, A. Narayan, Y. Liu, H. Zhang, Z. Ni, R. Liu, E. Sang Choi, A. Suslov, S. Sanvito, L. Pi, H.-Z. Lu, A. C. Potter, and F. Xiu, Quantum Hall effect based on Weyl orbits in Cd_3As_2, Nature (London) **565**, 331 (2019).

[49] S. Nishihaya, M. Uchida, Y. Nakazawa, R. Kurihara, K. Akiba, M. Kriener, A. Miyake, Y. Taguchi, M. Tokunaga, and M. Kawasaki, Quantized surface transport in topological Dirac semimetal films, Nat. Commun. **10**, 2564 (2019).

[50] T. Liang, Q. Gibson, M. N. Ali, M. Liu, R. J. Cava, and N. P. Ong, Ultrahigh mobility and giant magnetoresistance in the Dirac semimetal Cd_3As_2, Nat. Mater. **14**, 280 (2014).

[51] G. Zheng, M. Wu, H. Zhang, W. Chu, W. Gao, J. Lu, Y. Han, J. Yang, H. Du, W. Ning, Y. Zhang, and M. Tian, Recognition of Fermi-arc states through the magnetoresistance quantum oscillations in Dirac semimetal Cd_3As_2 nanoplates, Phys. Rev. B **96**, 121407(R) (2017).

[52] C. Wang, Y. Zhang, J. Huang, S. Nie, G. Liu, A. Liang, Y. Zhang, B. Shen, J. Liu, C. Hu, Y. Ding, D. Liu, Y. Hu, S. He, L. Zhao, L. Yu, J. Hu, J. Wei, Z. Mao, Y. Shi, X. Jia, F. Zhang, S. Zhang, F. Yang, Z. Wang, Q. Peng, H. Weng, X. Dai, Z. Fang, Z. Xu, C. Chen, and X. J. Zhou, Observation of Fermi arc and its connection with bulk states in the candidate type-II Weyl semimetal WTe_2, Phys. Rev. B **94**, 241119(R) (2016).

[53] P. Li, Y. Wen, X. He, Q. Zhang, C. Xia, Z. M. Yu, S. A. Yang, Z. Zhu, H. N. Alshareef, and X. X. Zhang, Evidence for topological type-II Weyl semimetal WTe_2, Nat. Commun. **8**, 2150 (2017).

[54] S. Roy, M. Kolodrubetz, J. E. Moore, and A. G. Grushin, Chern numbers and chiral anomalies in Weyl butterflies, Phys. Rev. B **94**, 161107(R) (2016).

[55] F. Abdulla, A. Das, S. Rao, and G. Murthy, Time-reversal-broken Weyl semimetal in the Hofstadter regime, SciPost Phys. Core **5**, 014 (2022).